JACS
JOURNAL OF THE AMERICAN CHEMICAL SOCIETY

Fine-Tuned Photoactive and Interconnection Layers for Achieving over 13% Efficiency in a Fullerene-Free Tandem Organic Solar Cell

Yong Cui,[†,‡] Huifeng Yao,[†,‡] Bowei Gao,[†,‡] Yunpeng Qin,[§] Shaoqing Zhang,[§] Bei Yang,[†,‡] Chang He,[†,‡] Bowei Xu,*[,†,‡] and Jianhui Hou*[,†,‡]

[†]State Key Laboratory of Polymer Physics and Chemistry, Beijing National Laboratory for Molecular Sciences, Institute of Chemistry, Chinese Academy of Sciences, Beijing 100190, China

[‡]University of Chinese Academy of Sciences, Beijing 100049, China

[§]School of Chemistry and Biology Engineering, University of Science and Technology Beijing, Beijing 100083, China

Supporting Information

ABSTRACT: Fabricating organic solar cells (OSCs) with a tandem structure has been considered an effective method to overcome the limited light absorption spectra of organic photovoltaic materials. Currently, the most efficient tandem OSCs are fabricated by adopting fullerene derivatives as acceptors. In this work, we designed a new non-fullerene acceptor with an optical band gap (E_g^{opt}) of 1.68 eV for the front subcells and optimized the phase-separation morphology of a fullerene-free active layer with an E_g^{opt} of 1.36 eV to fabricate the rear subcell. The two subcells show a low energy loss and high external quantum efficiency, and their photoresponse spectra are complementary. In addition, an interconnection layer (ICL) composed of ZnO and a pH-neutral self-doped conductive polymer, PCP-Na, with high light transmittance in the near-IR range was developed. From the highly optimized subcells and ICL, solution-processed fullerene-free tandem OSCs with an average power conversion efficiency (PCE) greater than 13% were obtained.

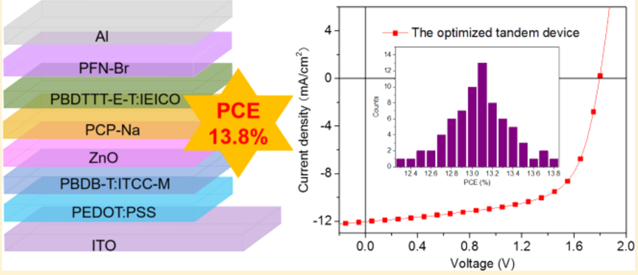

INTRODUCTION

Solution-processed organic solar cells (OSCs) in which the photoactive layers are composed of organic semiconductors have attracted considerable attention because of their advantages in enabling the fabrication of light-weight, large-area, flexible solar panels through low-cost printing technologies.[1−5] Because the optical absorption of organic semiconductors originates from the $\pi-\pi^*$ transition between the highest occupied molecular orbital (HOMO) and the lowest unoccupied molecular orbital (LUMO), these materials exhibit absorption peaks with narrow full width at half-maximum (fwhm), which limits the harvesting of sunlight. Therefore, constructing tandem OSCs by stacking two or more photoactive layers with complementary absorption spectra in series has been considered as an effective method to improve the light absorption.[6−8] To reduce the thermal loss in the subcells, the energy loss (E_{loss}) (which can be calculated by the equation $E_{loss} = E_g - eV_{OC}$, where E_g is the band gap of the subcells, e is the elementary charge, and V_{OC} is the open-circuit voltage[9−11]) should be as low as possible for each of the subcells to produce a higher V_{OC}. Thus, the search for organic photovoltaic materials that can yield higher V_{OC} relative to their band gaps has become one of the key strategies for advancing the power conversion efficiency (PCE) of tandem OSCs. Much effort has recently been devoted to solution-processed tandem OSCs,[12,13] and PCEs approaching or even exceeding 12% have been achieved.[14−17] However, although an E_{loss} as low as 0.6 eV has been realized in single-junction OSCs,[9,11,18−21] for all the reported efficient tandem OSCs, i.e., with PCEs around 12%,[14−17,22] the E_{loss} values for one or both of the subcells were higher than 0.7 eV, even approaching 0.9 eV, clearly indicating that there is still much room for improving the photovoltaic performance of tandem OSCs.

Along with the photoactive materials, the interconnection layer (ICL), which typically consists of a double-layer structure composed of a p-type and an n-type interlayer material between the two subcells, also plays a critical role in affecting the photovoltaic performance of tandem OSCs. The requirements for ICLs are as follows: (1) the p-type and n-type interlayers in an ICL should have excellent hole and electron collection abilities, respectively, and the collected holes and electrons must be recombined efficiently in the ICL; (2) the ICL should be highly transparent, particularly for sunlight in the long-wavelength range, to reserve more sunlight for the rear narrow-band-gap (NBG) subcells; and (3) the ICL should be sufficiently robust to protect the front subcells from erosion by the organic solvents used to fabricate the rear subcells. Currently, ICLs with a structure of ZnO/PEDOT:PSS, where ZnO refers to a zinc oxide layer and PEDOT:PSS is a layer of

Received: February 15, 2017
Published: May 12, 2017

DOI: 10.1021/jacs.7b01493
J. Am. Chem. Soc. XXXX, XXX, XXX−XXX

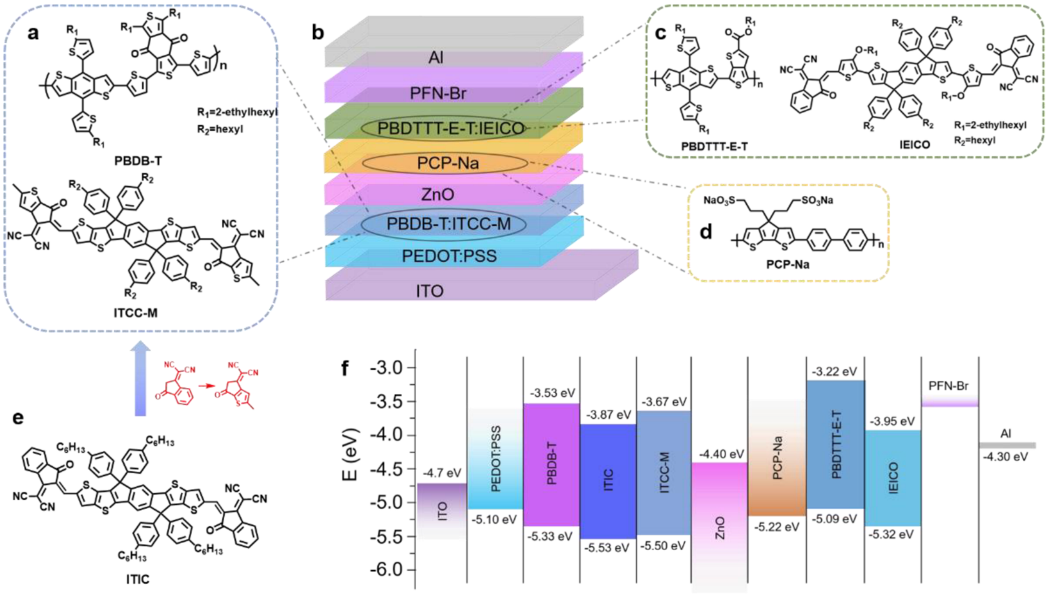

Figure 1. (a, c) Molecular structures of electron donor and electron acceptor materials in the (a) front and (c) rear cells. (d) Molecular structure of the interconnection layer, PCP-Na, in the tandem cells. (b) Device architecture of the tandem OSCs. (e) Molecular structure of ITIC. (f) Schematic energy level diagram of each material used in this study.

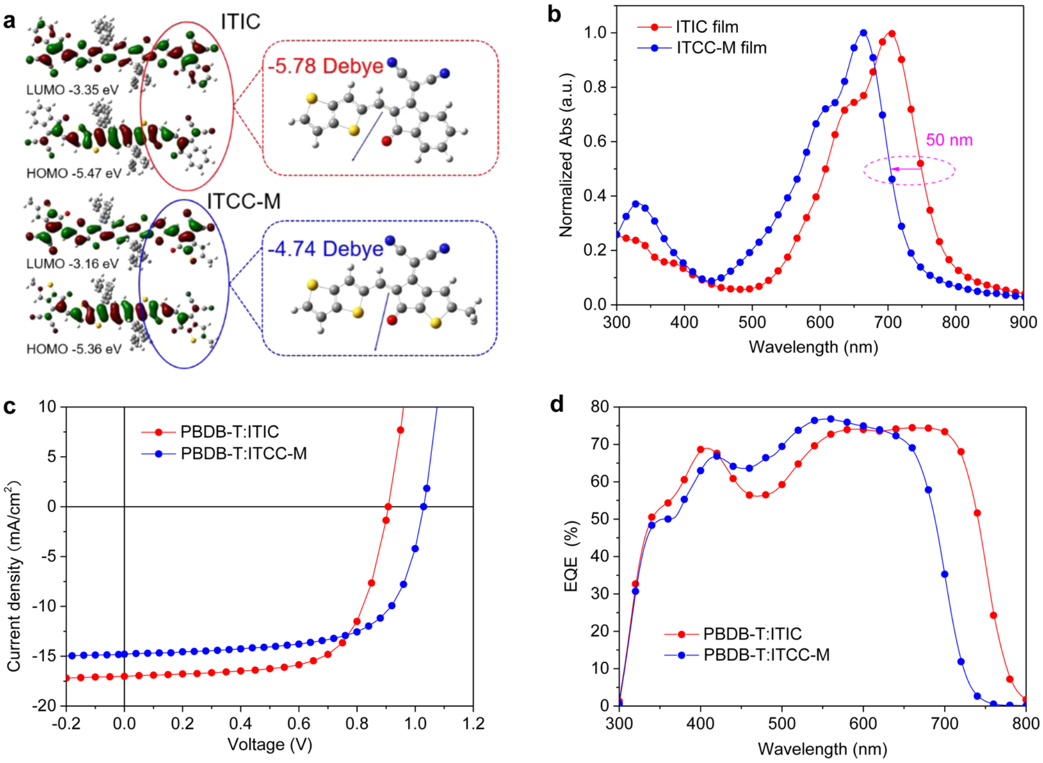

Figure 2. (a) HOMO and LUMO surfaces of ITIC and ITCC-M calculated at the B3LYP/6-31G(d,p) level. Insets: Dipole moments of the key segments in ITIC and ITCC-M. (b) Normalized absorption spectra of ITIC and ITCC-M. (c) *J*−*V* and (d) EQE curves of PBDB-T:ITIC and PBDB-T:ITCC-M OSCs.

pH-neutral poly(3,4-ethylenedioxythiophene):poly(styrenesulfonate), are broadly used in tandem OSCs. However, PEDOT:PSS has non-negligible optical absorption of sunlight in the deep-red and near-IR range[23] and thus may limit the external quantum efficiency (EQE) of the NBG rear subcells. Therefore, it is essential to employ another solution-processable p-type layer to replace the PEDOT:PSS in the ICL.

Recently, the study of fullerene-free OSCs, in which nonfullerene (NF) organic semiconductors are used to replace fullerene-based materials as electron acceptors, has attracted considerable interest. In addition, PCEs of over 11% have been achieved in single-junction fullerene-free OSCs.[24−27] Fullerene-free OSCs often have much lower E_{loss} than fullerene-based OSCs. For instance, the most efficient fullerene-based single-junction OSC, with a PCE of 11.7% as reported by Yan and co-

Table 1. Photovoltaic Parameters of Single-Junction OSCs Based on PBDT-T:ITIC, PBDB-T:ITCC-M, and PBDTTT-E-T:IEICO Active Layers and the Device Performances of PBDTTT-E-T:IEICO-Based OSCs with Different Anode Interfacial Layers

active layer	interface	V_{OC} (V)[a]	J_{SC} (mA/cm^2)[a]	J_{cal} (mA/cm^2)[b]	FF[a]	PCE (%)[a]
PBDB-T:ITIC	PEDOT:PSS	0.914 ± 0.005 (0.908)	16.5 ± 0.3 (17.0)	16.5	0.669 ± 0.023 (0.672)	10.1 ± 0.2 (10.4)
PBDB-T:ITCC-M	PEDOT:PSS	1.03 ± 0.003 (1.03)	14.5 ± 0.2 (14.8)	14.4	0.657 ± 0.005 (0.663)	9.83 ± 0.14 (10.1)
PBDTTT-E-T:IEICO	PEDOT:PSS	0.810 ± 0.003 (0.814)	17.4 ± 0.3 (17.8)	17.4	0.569 ± 0.016 (0.583)	8.02 ± 0.31 (8.45)
	PCP-Na	0.813 ± 0.004 (0.817)	18.5 ± 0.3 (18.8)	18.3	0.594 ± 0.007 (0.603)	8.93 ± 0.17 (9.26)
	PCP-Na[c]	0.819 ± 0.003 (0.823)	18.6 ± 0.3 (18.8)	18.2	0.651 ± 0.010 (0.667)	9.91 ± 0.25 (10.3)
	PCP-Na[d]	0.832 ± 0.003 (0.834)	13.2 ± 0.3 (13.8)	13.3	0.592 ± 0.009 (0.603)	6.53 ± 0.28 (6.96)

[a] The values in parentheses stand for the optimal results, and the statistical results are listed outside of the parentheses. The average values of the parameters were calculated from more than 10 independent cells. [b] Obtained by integration of the EQE curves. [c] The active layer was exposed to CB vapor for 1 min. [d] The active layer was exposed to CB vapor for 4 min.

workers,[28] showed a large E_{loss} of 0.8 eV, while E_{loss} values of 0.6 eV or even lower have been demonstrated in fullerene-free OSCs by several other research groups.[9,29−31] Clearly, in terms of reducing E_{loss}, fullerene-free active layers are better suited than their fullerene-based counterparts. However, the PCEs of the fullerene-free tandem OSCs are still much lower than those of the fullerene-based analogues.[32,33] The main obstacle is that the optical band gaps (E_g^{opt}) of the reported high-performance fullerene-free active layers are mostly between 1.5 and 1.6 eV,[34−36] which is too narrow for these materials to serve as the wide band gap (WBG) front subcell and too large for the NBG rear subcell. In this study, to demonstrate the superior potential of the fullerene-free active layers for use in highly efficient tandem OSCs, we designed a new NF acceptor with E_g^{opt} = 1.68 eV for the WBG subcell and optimized the phase-separation morphology of a fullerene-free active layer with E_g^{opt} = 1.36 eV for the NBG subcell. Then we fabricated fullerene-free tandem OSCs by employing an ICL based on ZnO and a pH-neutral and self-doped conductive polymer. Because both subcells show a low E_{loss} and high EQE and the ICL is highly transparent in the near-IR range, the resulting double-junction fullerene-free tandem OSCs demonstrate an outstanding PCE of over 13%, the highest value reported for OSCs to date.

■ RESULTS AND DISCUSSION

First, to obtain a suitable small-molecule (SM) NF acceptor for the WBG front cells, we designed and synthesized a new acceptor, 3,9-bis((*Z*)-1-(6-(dicyanomethylene)-2-methyl-5,6-dihydro-6*H*-cyclopenta[*b*]thiophen-6-one-5-yl)ethylene)-5,5,11,11-tetrakis(4-hexylphenyl)dithieno[2,3-*d*:2′,3′-*d*′]-*s*-indaceno[1,2-*b*:5,6-*b*′]dithiophene (ITCC-M). As shown in Figure 1a, ITCC-M is a derivative of a well-known SM NF acceptor, 3,9-bis(2-methylene-(3-(1,1-dicyanomethylene)-indanone)-5,5,11,11-tetrakis(4-hexylphenyl)dithieno[2,3-*d*:2′,3′-*d*′]-*s*-indaceno[1,2-*b*:5,6-*b*′]dithiophene (ITIC). As shown in Figure 2b, the absorption spectrum of the ITIC film features an absorption edge at 790 nm. Although single-junction OSCs using ITIC as the acceptor and the polymer poly[(2,6-(4,8-bis(5-(2-ethylhexyl)thiophen-2-yl)benzo[1,2-*b*:4,5-*b*′]dithiophene)-*co*-(1,3-bis(5-thiophene-2-yl)-5,7-bis(2-ethylhexyl)benzo[1,2-*c*:4,5-*c*]dithiophene-4,8-dione)] (PBDB-T) as the donor yielded PCEs of over 10% accompanied by a low E_{loss} of 0.66 eV, the absorption band of the PBDB-T:ITIC blend is too narrow to be used in the front WBG subcells. From the perspective of molecular design, the low E_g^{opt} of ITIC is attributable to the strong intermolecular charge transfer (ICT) effect between its electron-rich central segment and the electron-withdrawing end groups; thus, its absorption spectrum may be blue-shifted by weakening the ICT effect.[37−42] As shown in Figure 1e, ITCC-M was designed by replacing the phenyl rings in the end groups by α-methylthiophene groups. As shown in Figure 2a, the dipole moments of the key segments in ITIC and ITCC-M are −5.78 and −4.74 D, respectively, implying that the ICT effect in ITCC-M is weaker than that in ITIC.

Relative to ITIC, the E_g^{opt} of ITCC-M is enlarged by approximately 0.11 eV (Figure 2b). Cyclic voltammetry (CV) measurements (Figure S6) indicate that the enlarged band gap of ITCC-M is due mainly to its elevated LUMO level, which implies that a higher V_{OC} can be expected in the PBDB-T:ITCC-M-based OSCs. As shown in Figure 2b, in going from the ITIC curve to the ITCC-M curve, the half-peak-height position in the long-wavelength direction is shifted from 750 to 700 nm. Therefore, when ITCC-M is used as the front WBG subcell instead of ITIC, the solar photon flux from 700 to 750 nm, which can theoretically give a current density of 2.48 mA/cm^2 (calculated for an overall EQE of 70%; Figure S7), can be reserved for the NBG rear subcell, which is beneficial for obtaining the symmetrically high current density in the tandem OSCs.

Two types of single-junction OSCs with a device architecture of ITO/PEDOT:PSS/active layer/PFN-Br/Al were fabricated using the PBDB-T:ITIC and PBDB-T:ITCC-M blends. Here we adopted the optimal active layer fabrication condition to fabricate the PBDB-T:ITIC device, referring to the reported study.[24] The photovoltaic characteristics of the two devices were measured under the illumination of simulated solar light (AM 1.5G, 100 mW/cm^2); the representative current density−voltage ($J-V$) curves are shown in Figure 2c. The corresponding photovoltaic parameters are listed in Table 1. Relative to the PBDB-T:ITIC devices, the PBDB-T:ITCC-M devices demonstrate significantly improved V_{OC}, i.e., from 0.914 ± 0.005 to 1.03 ± 0.003 V. In the EQE measurements (Figure. 2d), relative to the PBDB-T:ITIC device, the photoresponse spectrum of the PBDB-T:ITCC-M device is blue-shifted by 50 nm. Clearly, relative to the PBDB-T:ITIC device, the PBDB-T:ITCC-M device exhibits a narrower photoresponse spectrum with an enhanced EQE in the short-wavelength range from 420 to 600 nm, a higher V_{OC}, and a similar PCE. These results suggest that PBDB-T:ITCC-M is highly suitable for use in the fabrication of the WBG front subcell of the tandem OSCs.

To fabricate the NBG rear cells, we selected the blend of 2,2′-((2*Z*,2′*Z*)-((5,5′-bis(4,4,9,9-tetrakis(4-hexylphenyl)-4,9-dihydro-*s*-indaceno[1,2-*b*:5,6-*b*′]dithiophene-2,7-diyl)bis(4-((2-ethylhexyl)oxy)thiophene-5,2-diyl))bis(methanylylidene))bis-(3-oxo-2,3-dihydro-1*H*-indene-2,1-diylidene))dimalononitrile

DOI: 10.1021/jacs.7b01493

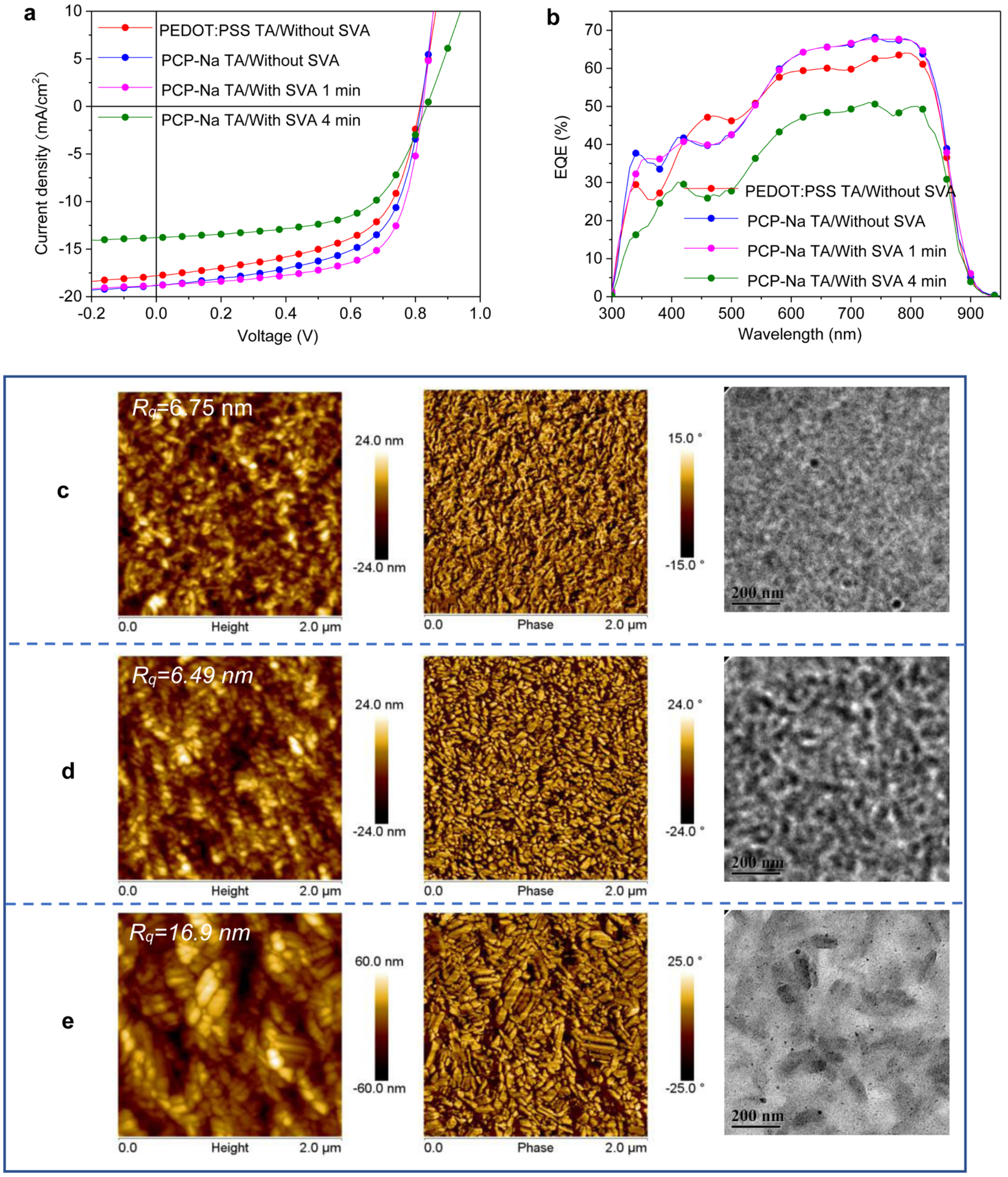

Figure 3. (a) *J*–*V* curves and (b) EQE spectra of PBDTTT-E-T:IEICO OSCs fabricated under different conditions. (c–e) AFM topography images (2 μm × 2 μm), AFM phase images (2 μm × 2 μm), and TEM images of the blend film of PBDTTT-E-T:IEICO (c) without SVA, (d) upon exposure to CB vapor for 1 min, and (e) upon exposure to CB vapor for 4 min.

(IEICO) and the well-known polymer donor PBDTTT-E-T (Figure 1c) as the candidate. Although the PBDTTT-E-T:IEICO-based device exhibited a broad photoresponse spectrum extending to 900 nm and demonstrated a low E_{loss} of 0.52 eV, the device performance was significantly limited because of the low fill factor (FF) and short circuit current density (J_{SC}).[18] To enhance these two factors, two strategies were adopted in this study.

First, because the photoresponse of the PBDTTT-E-T:IEICO device is mainly located in the deep-red and near-IR range, where the commonly used p-type buffer layer PEDOT:PSS has non-negligible absorption, we used a self-doped p-type conductive polymer, PCP-Na, to replace the PEDOT:PSS to construct the buffer layer between the indium tin oxide (ITO) and the active layer because PCP-Na is more transparent than PEDOT:PSS in the range beyond 525 nm (Figure S9).[43] As demonstrated in Figure 3b, under the same device fabrication conditions, the PCP-Na-modified device shows a slightly lower EQE below 525 nm but an improved EQE beyond 600 nm relative to the PEDOT:PSS-modified device. As a result, the J_{SC} of the PCP-Na-modified device can be improved from 17.4 ± 0.3 to 18.5 ± 0.3 mA/cm^2.

We then used several methods to optimize the phase separation morphology of the PBDTTT-E-T:IEICO blend film to improve the FF and found that the solvent-vapor annealing (SVA) method[22,44−46] was very effective. We optimized the SVA process by adopting a few types of solvents, including chloroform, tetrahydrofuran, chlorobenzene (CB), and toluene. Among all of these organic solvents, the device treated with CB vapor exhibited the best photovoltaic performance (Table S3). As shown in Figure 3a, after treatment with CB vapor for 1 min, the FF of the device greatly improved from 0.594 ± 0.007 to 0.651 ± 0.010 (Table 1); however, when the SVA time was prolonged to 4 min, both the J_{SC} and FF of the device were

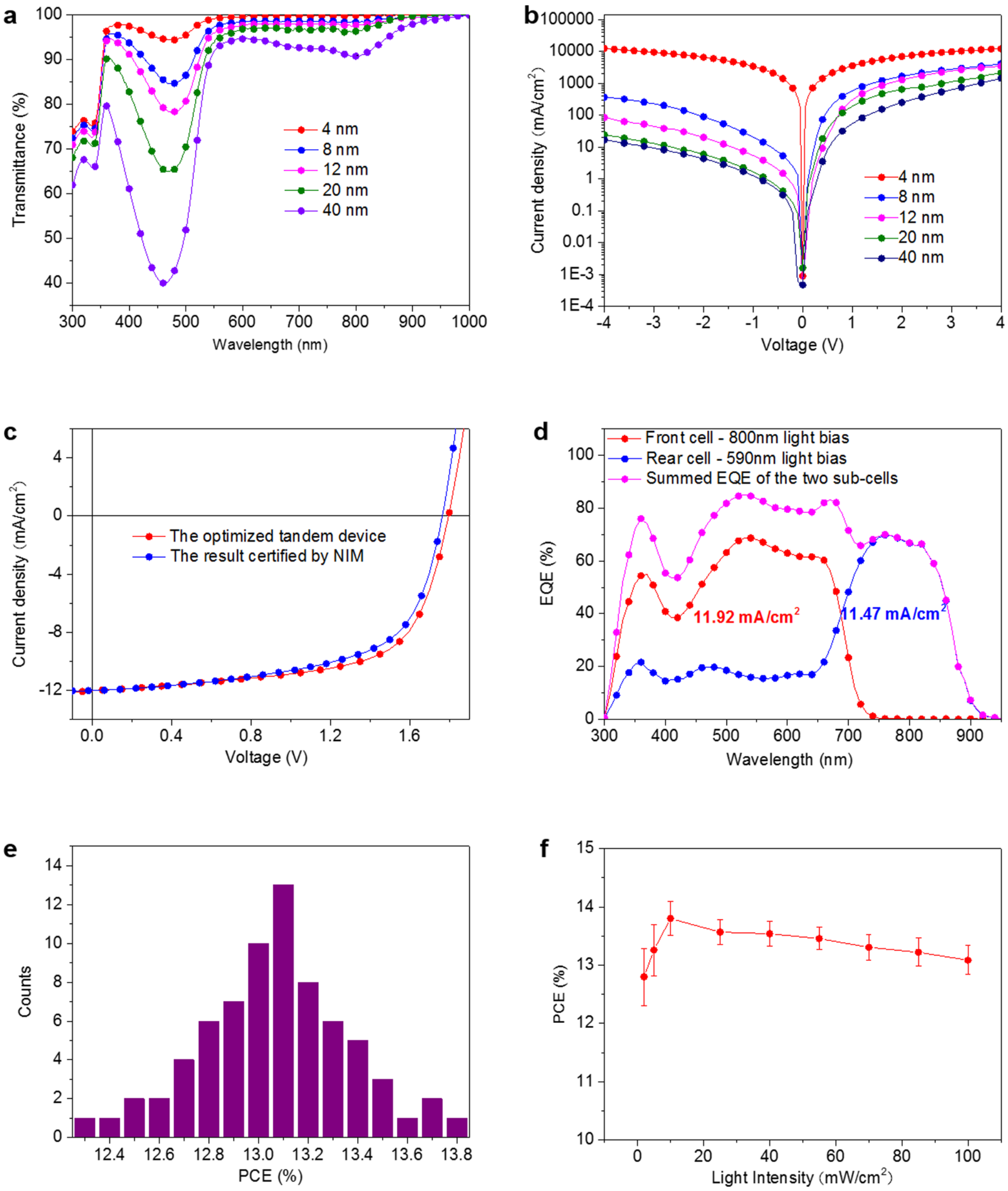

Figure 4. (a) Transmission spectra of ZnO/PCP-Na ICLs with different PCP-Na thicknesses. (b) Diode characteristic curves of ZnO/PCP-Na devices. (c) $J-V$ curves and (d) EQE spectra of front and rear subcells and calculated EQE of the tandem cell based on the summed EQE spectra of the subcells. (e) Histogram of PCE counts for 72 individual cells. (f) PCE of the tandem OSCs as a function of incident light intensity.

significantly reduced. According to the results obtained from atomic force microscopy (AFM) and transmission electron microscopy (TEM) measurements (Figure 3c−e), the surface roughness of the blend film is nearly unchanged after the 1 min SVA treatment, but a strong phase separation can be distinguished in the AFM phase image, and nanoscale wormlike aggregations can be observed in the TEM image; when the blend film is treated for a longer time, we observe numerous large size crystals (Figure 3e), which should be ascribed to the aggregation of IEICO. Overall, after the two-step optimization, the PCE of the PBDTT-ET:IEICO-based device was significantly enhanced from 8.02 ± 0.31% to 9.91 ± 0.25%. More importantly, the higher EQE in the long-wavelength region, the favorable FF, and the low E_{loss} make it very suitable for use in the NBG subcells in the tandem OSCs.

Furthermore, to achieve efficient tandem OSCs, a solution-processable ICL with the aforementioned properties is still required. Here, an ICL with a bilayer structure of ZnO/PCP-Na is used. Since ZnO is highly transparent and has favorable electron collection abilities, the key problem in this study is to determine the optimal thickness of the PCP-Na layer. As shown by the transmission spectra of ZnO/PCP-Na (Figure 4a), thicker PCP-Na will cause stronger light absorption. To identify the optimal thickness of PCP-Na, we fabricated the devices with a structure of ITO/ZnO/PCP-Na/Au and then measured the $J-V$ characteristics. As shown in Figure 4b, the devices with comparatively thicker PCP-Na layers (≥12 nm) show favorable diode characteristics, i.e., low leakage current densities and high rectification ratios, implying that the charge injection and recombination are efficient; however, for the devices with PCP-Na layers thinner than 12 nm, the leakage is higher and the rectification ratio is lower. Therefore, when the diode characteristics and the transmission properties are taken into

DOI: 10.1021/jacs.7b01493

Table 2. Photovoltaic Performance Parameters of Reference Subcells and Tandem OSCs

	thickness (nm)	V_{OC} (V)[a]	J_{SC} (mA/cm^2)[a]	FF	PCE (%)[a]
front cell	130	1.00 ± 0.005 (1.00)	13.9 ± 0.3 (14.0)	0.648 ± 0.007 (0.653)	9.01 ± 0.12 (9.14)[b]
rear cell	120	0.815 ± 0.004 (0.813)	19.2 ± 0.2 (19.4)	0.642 ± 0.010 (0.647)	10.1 ± 0.1 (10.2)[b]
tandem	130/120	1.79 ± 0.007 (1.80)	11.4 ± 0.3 (12.0)	0.641 ± 0.014 (0.639)	13.1 ± 0.3 (13.8)[c]

[a] Statistical and optimal results are listed outside of parentheses and in parentheses, respectively. [b] The average parameters were calculated from more than 10 independent cells. [c] The average parameters were calculated from 72 independent cells.

consideration, the optimal thickness of PCP-Na should be between 12 and 20 nm.

Using the fully optimized WBG and NBG active layers and the ICL, we fabricated the double-junction tandem OSCs with the structure shown in Figure 1b. Initially, we scanned the thicknesses of the WBG and NBG active layers in the tandem devices and obtained their optimal thicknesses (Table S4). The V_{OC} of the tandem device fabricated under the optimized conditions is almost equal to the sum of the values for the single-junction subcells of PBDB-T:ITCC-M and PBDTTT-E-T:IEICO, implying that the ICL layer performs very well (Figure 4c and Table 2). Under bias illumination, the EQE spectra of the individual subcells were measured both with and without application of an electrical bias.[47,48] The subcells exhibit similar EQE responses regardless of whether the electrical bias is applied (Figure S11). The integral current densities obtained from the EQE measurements are 11.92 mA/cm^2 for the front subcell and 11.47 mA/cm^2 for the rear subcell, which are symmetric and very similar to that of the tandem device in J−V measurement. Moreover, the calculated EQE based on the summed EQE spectra of the two subcells provides an overall estimate of the photon-to-current efficiency in the tandem device, which reached 70−80% over the entire response range (Figure 4d). Under the illumination of simulated solar light (AM 1.5G, 100 mW/cm^2), the tandem cells showed an average PCE of 13.1 ± 0.3%, with a best value of 13.8%. The photovoltaic performance of the best tandem device was certified by the National Metrology Institute (NMI), and a certified PCE of 13.0% was obtained (Figure S12). The lower PCE certified by the NMI is due mainly to the decreased FF, which is most likely caused by the intense UV irradiation of the device during the encapsulation process (Figure S13). Figure 4e presents a PCE histogram of 72 cells fabricated in two batches; over 65% of the cells exhibited PCE values exceeding 13%.

Since solar irradiation varies throughout the daytime and the solar cells mostly work under an illumination of less than 1 sun, evaluating the photovoltaic performance of the tandem device under varied illumination intensities is also important. As shown in Figure 4f, the device shows an increase in PCE with a gradual reduction of light intensity from 100 to 10 mW/cm^2, below which the PCE then drops with further reduced light intensity. As shown in Table S6, the device with a PCE of 13.4% under standard AM 1.5G illumination achieves a PCE of 14.1% under 10 mW/cm^2, which implies that the tandem device can work effectively under different irradiation conditions.

CONCLUSIONS

We have demonstrated a highly efficient fullerene-free double-junction tandem OSC by fully optimizing the active layers in the two subcells and the ICL. For the WBG front subcell, a new SM NF acceptor, ITCC-M, was designed to realize a narrower absorption spectrum with a high V_{OC}; for the NBG rear subcell, the anode buffer layer and the phase-separation morphology of the active layer were optimized to achieve a high EQE in the near-IR range and satisfactory FF, respectively. By adopting an ICL with an optimized thickness to achieve efficient charge collection and recombination and high light transmittance, we were able to fabricate tandem cells with PCEs of 13−14% under an illumination of 0.02−1 sun.

Overall, this work not only demonstrates a systematic study to achieve an outstanding photovoltaic result but also reveals the superior properties of fullerene-free tandem OSCs. Since the overall EQE of the best device is not very high (i.e., below 80% in most of the response range; Figure 4d) and the FF is only 0.639, there is still much room for further improvement in the photovoltaic performance. Benefiting from the highly tunable optoelectronic properties of the fullerene-free photoactive layer materials, a much higher PCE can be expected for fullerene-free tandem OSCs.

EXPERIMENTAL SECTION

Single Solar Cell Fabrication. Single solar cells based on PBDB-T:ITCC-M were fabricated with the conventional device structure of glass/ITO/PEDOT:PSS/PBDB-T:ITCC-M/PFN-Br/Al. A PEDOT:PSS layer (Clevios P VP AI. 4083) with a thickness of about 30 nm was spin-coated on the precleaned ITO substrate at 4000 rpm for 40 s and annealed at 150 °C for 20 min. A 1:1 mixture of PBDB-T and ITCC-M was fully dissolved in CB with a total concentration of 20 mg/mL and stirred at 40 °C for 2 h. Before spin-coating, 1,8-iodooctane (1% v/v) was added to the mixture. Subsequently, the active layer was spin-coated on the PEDOT:PSS at 2500 rpm for 1 min, and the film was treated by thermal annealing at 100 °C. For PBDTTT-E-T:IEICO, single solar cells with the conventional device structure of glass/ITO/PEDOT:PSS or PCP-Na/PBDTTT-E-T:IEICO/PFN-Br/Al were fabricated. A PCP-Na (6 nm) or PEDOT:PSS (30 nm) layer was spin-coated on the precleaned ITO substrate and annealed at 150 °C for 20 min. PCP-Na was dissolved in a 3:7 mixture of water and methanol. The active layer was fabricated according to previous reports.[18] In the case of PBDTTT-E-T:IEICO, some devices had to be treated by solvent-vapor annealing for different times. A PFN-Br layer with a thickness of about 5 nm was spin-coated on the top of all of the active layers at 3000 rpm for 30 s. PFN-Br was dissolved in methanol at a concentration of 0.5 mg/mL. Finally, a 100 nm thick layer of Al was deposited under high vacuum (ca. 3 × 10^{-4} Pa). PBDB-T and IEICO were purchased from Solarmer Materials Inc.

Tandem Solar Cell Fabrication. Tandem solar cells were fabricated with the conventional device structure of glass/PEDOT:PSS/PBDB-T:ITCC-M/ZnO/PCP-Na/PBDTTT-E-T:IEICO/PFN-Br/Al. The front cell was fabricated via the same process as the single cells, with an active layer thickness of about 130 nm (1500 rpm for 1 min). Subsequently, the ZnO nanoparticle layer (30 nm) was spin-coated on top of the active layer of the front cell, and the film was treated by thermal annealing at 100 °C for 10 min. ZnO nanoparticles were synthesized by the previously reported method.[49] Then a PCP-Na layer with a thickness of 12−15 nm (4 mg/mL, 3000 rpm for 30 s) was spin-coated on top of the ZnO layer in the air, and the film was treated by thermal annealing at 100 °C for 10 min in the glovebox. The rear cell was fabricated via the same process as the single cells, with active layer thickness of about 120 nm. A ca. 5 nm thick PFN-Br layer was spin-coated on the top of all of the active

DOI: 10.1021/jacs.7b01493
J. Am. Chem. Soc. XXXX, XXX, XXX−XXX

layers. Finally, 100 nm thick Al layer was deposited under high vacuum (ca. 3× 10^{-4} Pa).

Device Characterization and Measurement. The *J*−*V* curves of devices were measured under a 100 mW/cm^2 AM 1.5G light source using a AAA solar simulator (XES-70S1, SAN-EI Electric Co., Ltd.) with a spectral mismatch factor of 1.01, calibrated by the National Institute of Metrology (NIM), China. Before each test, the solar simulator was calibrated with a standard Si solar cell (made by Enli Technology Co., Ltd., Taiwan, and calibrated by NIM). In order to investigate the dependence of the device performance on the light intensity, a neutral density sieve was used to tune the light intensity, and a standard Si solar cell was used to calibrate the light intensity. The EQE spectrum was measured using a QE-R3011 Solar Cell Spectral Response Measurement System (Enli Technology Co., Ltd., Taiwan). For the EQE measurements with applied electrical bias, electrical biases of 0.7 and 0.9 V were applied on the tandem OSCs to measure the front and rear subcells, respectively. The effective area of the device was defined as 3.68 mm^2 in our group. The optimized device was sent to NIM for certification. The mismatch factors (MMFs) for the front and rear cells are 0.9922 and 1.0080, respectively.

Synthesis. The chemical structure and synthetic route for ITCC-M are shown in Figure S1. Compound **1** was purchased from Alfa and compound **5** from Solarmer Materials Inc.

*5-Methylthiophene-2-carbonyl Chloride (**2**).* To a solution of compound **1** (2.82 g, 20 mmol) in 50 mL of chloroform was added thionyl chloride (9.44 g, 80 mmol) under the protection of an inert gas, and then 5 drops of dry DMF was added to the reaction mixture. After 1 h of stirring at 65 °C, the excess thionyl chloride was removed by distillation under reduced pressure to afford compound **2**, which was used without further purification.

*2-Methyl-4H-cyclopenta[b]thiophene-4,6(5H)-dione (**3**).* Malonyl dichloride (12 g, 90 mmol) was added to a solution of $AlCl_3$ in dry dichloromethane (50 mL). After this mixture was flushed with inert gas for 10 min, compound **2** (20 mmol) was added, and the reaction mixture was stirred at 60 °C overnight and then cooled to room temperature. The reaction mixture was poured into oxalic acid solution (10%), and the pH of the resulting solution was tuned to below 7. The product (1 g, 30% yield) was extracted by dichloromethane as a yellow solid. EI-MS: *m*/*z* calcd for $C_8H_6O_2S$, 166.19; found, 166.01. ^{1}H NMR ($CDCl_3$, 400 MHz), δ (ppm): 7.05 (d, 1H), 3.36 (s, 2H), 2.64 (s, 3H). ^{13}C NMR ($CDCl_3$, 400 MHz), δ (ppm): 190.38, 188.08, 158.78, 158.32, 154.45, 118.78, 48.61, 16.87.

*2-(2-Methyl-6-oxo-5,6-dihydro-4H-cyclopenta[b]thiophen-4-ylidene)malononitrile (**4**).* Compound **3** (1 g, 6 mmol) and malononitrile (0.59 g, 9 mmol) were added to 50 mL of dimethyl sulfoxide, and sodium acetate (0.74 g, 9 mmol) was added to the reaction mixture. After 1 h of stirring at room temperature, the mixture was poured into 50 mL of water. The resulting mixture was acidified to pH 1−2 with HCl (10%), and then the solid was filtered. The crude product was purified by column chromatography to yield compound **4** as a yellow solid (1.09 g, 85% yield). EI-MS: *m*/*z* calcd for $C_{11}H_6N_2OS$, 214.24; found, 214.02. ^{1}H NMR ($CDCl_3$, 400 MHz), δ (ppm): 7.56 (d, 1H), 3.82 (s, 2H), 2.69 (s, 3H). ^{13}C NMR ($CDCl_3$, 400 MHz), δ (ppm): 185.30, 161.44, 159.60, 156.12, 150.24, 120.60, 112.08, 111.69, 45.94, 17.14.

ITCC-M. Compound **5** (108 mg, 0.1 mmol) and compound **4** (86 mg, 0.4 mmol) were added to a mixture of chloroform (10 mL) and pyridine (0.1 mL), and then the reaction mixture was placed in a microwave reactor (dynamic models, 70 °C, 100 W) and stirred for 2 h. The mixture was directly purified by silica gel column chromatography with dichloromethane as the eluent to obtain the product as a black solid (120 mg, 82% yield). MALDI-TOF: *m*/*z* calcd for $C_{92}H_{82}N_4O_2S_6$, 1466.48; found, 1467.4 $(M + H)^+$. ^{1}H NMR ($CDCl_3$, 400 MHz), δ (ppm): 8.56 (d, 1H), 5.71 (s, 1H), 8.08 (s, 1H), 7.63 (s, 1H), 7.60 (s, 1H), 7.18 (d, 4H), 7.13 (d, 4H), 2.66 (s, 3H), 2.51 (t, 4H), 1.55 (m, 4H), 1.31 (m, 12H), 0.84 (s, 6H). ^{13}C NMR ($CDCl_3$, 400 MHz), δ (ppm): 180.48, 156.88, 156.60, 155.32, 152.77, 151.31, 147.45, 146.70, 145.66, 142.99, 142.38, 139.16, 138.52, 136.79, 135.55, 135.37, 128.82, 127.94, 125.15, 121.66, 118.28, 114.34, 113.80, 68.99, 63.21, 35.63, 31.73, 31.26, 29.21, 22.61, 22.61, 17.05, 14.11.

■ ASSOCIATED CONTENT

Ⓢ Supporting Information

The Supporting Information is available free of charge on the ACS Publications website at DOI: 10.1021/jacs.7b01493.

Synthetic route for ITCC-M, NMR spectra, CVs for ITIC and ITCC-M, photovoltaic data, and certificate results for the tandem OSCs (PDF)

■ AUTHOR INFORMATION

Corresponding Authors

*xubowei2004@iccas.ac.cn
*hjhzlz@iccas.ac.cn

ORCID

Huifeng Yao: 0000-0003-2814-4850
Chang He: 0000-0002-9804-5455
Bowei Xu: 0000-0001-6467-6147
Jianhui Hou: 0000-0002-2105-6922

Notes

The authors declare no competing financial interest.

■ ACKNOWLEDGMENTS

The authors acknowledge the financial support from the National Natural Science Foundation of China (Grants 91333204, 21325419, 21504095) and the Chinese Academy of Sciences (Grant XDB12030200).

■ REFERENCES

(1) Kaltenbrunner, M.; White, M. S.; Glowacki, E. D.; Sekitani, T.; Someya, T.; Sariciftci, N. S.; Bauer, S. *Nat. Commun.* **2012**, *3*, 770.

(2) Søndergaard, R.; Hösel, M.; Angmo, D.; Larsen-Olsen, T. T.; Krebs, F. C. *Mater. Today* **2012**, *15*, 36−49.

(3) Zhou, Y.; Fuentes-Hernandez, C.; Khan, T. M.; Liu, J. C.; Hsu, J.; Shim, J. W.; Dindar, A.; Youngblood, J. P.; Moon, R. J.; Kippelen, B. *Sci. Rep.* **2013**, *3*, 1536.

(4) Krebs, F. C. *Sol. Energy Mater. Sol. Cells* **2009**, *93*, 394−412.

(5) Yu, G.; Gao, J.; Hummelen, J. C.; Wudl, F.; Heeger, A. J. *Science* **1995**, *270*, 1789−1791.

(6) Dou, L.; You, J.; Yang, J.; Chen, C.-C.; He, Y.; Murase, S.; Moriarty, T.; Emery, K.; Li, G.; Yang, Y. *Nat. Photonics* **2012**, *6*, 180−185.

(7) Yusoff, A. R. b. M.; Kim, D.; Kim, H. P.; Shneider, F. K.; da Silva, W. J.; Jang, J. *Energy Environ. Sci.* **2015**, *8*, 303−316.

(8) Dennler, G.; Scharber, M. C.; Ameri, T.; Denk, P.; Forberich, K.; Waldauf, C.; Brabec, C. J. *Adv. Mater.* **2008**, *20*, 579−583.

(9) Liu, J.; Chen, S.; Qian, D.; Gautam, B.; Yang, G.; Zhao, J.; Bergqvist, J.; Zhang, F.; Ma, W.; Ade, H.; Inganäs, O.; Gundogdu, K.; Gao, F.; Yan, H. *Nat. Energy* **2016**, *1*, 16089.

(10) Yao, J.; Kirchartz, T.; Vezie, M. S.; Faist, M. A.; Gong, W.; He, Z.; Wu, H.; Troughton, J.; Watson, T.; Bryant, D.; Nelson, J. *Phys. Rev. Appl.* **2015**, *4*, 014020.

(11) Zhang, H.; Li, S.; Xu, B.; Yao, H.; Yang, B.; Hou, J. *J. Mater. Chem. A* **2016**, *4*, 18043−18049.

(12) Lu, S.; Guan, X.; Li, X.; Sha, W. E. I.; Xie, F.; Liu, H.; Wang, J.; Huang, F.; Choy, W. C. H. *Adv. Energy Mater.* **2015**, *5*, 1500631.

(13) Gao, Y.; Le Corre, V. M.; Gaitis, A.; Neophytou, M.; Hamid, M. A.; Takanabe, K.; Beaujuge, P. M. *Adv. Mater.* **2016**, *28* (17), 3366−3373.

(14) Zheng, Z.; Zhang, S.; Zhang, J.; Qin, Y.; Li, W.; Yu, R.; Wei, Z.; Hou, J. *Adv. Mater.* **2016**, *28*, 5133−5138.

(15) Li, M.; Gao, K.; Wan, X.; Zhang, Q.; Kan, B.; Xia, R.; Liu, F.; Yang, X.; Feng, H.; Ni, W.; Wang, Y.; Peng, J.; Zhang, H.; Liang, Z.; Yip, H.-L.; Peng, X.; Cao, Y.; Chen, Y. *Nat. Photonics* **2017**, *11*, 85−90.

(16) Zhang, Q.; Wan, X.; Liu, F.; Kan, B.; Li, M.; Feng, H.; Zhang, H.; Russell, T. P.; Chen, Y. *Adv. Mater.* **2016**, *28*, 7008−7012.

(17) Zhou, H.; Zhang, Y.; Mai, C. K.; Collins, S. D.; Bazan, G. C.; Nguyen, T. Q.; Heeger, A. J. *Adv. Mater.* **2015**, *27*, 1767−1773.

(18) Yao, H.; Chen, Y.; Qin, Y.; Yu, R.; Cui, Y.; Yang, B.; Li, S.; Zhang, K.; Hou, J. *Adv. Mater.* **2016**, *28*, 8283−8287.

(19) Cheng, P.; Zhang, M.; Lau, T. K.; Wu, Y.; Jia, B.; Wang, J.; Yan, C.; Qin, M.; Lu, X.; Zhan, X. *Adv. Mater.* **2017**, *29*, 1605216.

(20) Gao, K.; Li, L.; Lai, T.; Xiao, L.; Huang, Y.; Huang, F.; Peng, J.; Cao, Y.; Liu, F.; Russell, T. P.; Janssen, R. A. J.; Peng, X. *J. Am. Chem. Soc.* **2015**, *137*, 7282−7285.

(21) Kawashima, K.; Tamai, Y.; Ohkita, H.; Osaka, I.; Takimiya, K. *Nat. Commun.* **2015**, *6*, 10085.

(22) Zhang, K.; Gao, K.; Xia, R.; Wu, Z.; Sun, C.; Cao, J.; Qian, L.; Li, W.; Liu, S.; Huang, F.; Peng, X.; Ding, L.; Yip, H. L.; Cao, Y. *Adv. Mater.* **2016**, *28*, 4817−4823.

(23) Xu, B.; Zheng, Z.; Zhao, K.; Hou, J. *Adv. Mater.* **2016**, *28*, 434−439.

(24) Zhao, W.; Zhang, S.; Hou, J. *Sci. China: Chem.* **2016**, *59*, 1574−1582.

(25) Yang, Y.; Zhang, Z. G.; Bin, H.; Chen, S.; Gao, L.; Xue, L.; Yang, C.; Li, Y. *J. Am. Chem. Soc.* **2016**, *138*, 15011−15018.

(26) Bin, H.; Gao, L.; Zhang, Z. G.; Yang, Y.; Zhang, Y.; Zhang, C.; Chen, S.; Xue, L.; Yang, C.; Xiao, M.; Li, Y. *Nat. Commun.* **2016**, *7*, 13651.

(27) Zheng, Z.; Zhang, S.; Zhang, J.; Qin, Y.; Li, W.; Yu, R.; Wei, Z.; Hou, J. *Adv. Mater.* **2016**, *28*, 5133−5138.

(28) Zhao, J.; Li, Y.; Yang, G.; Jiang, K.; Lin, H.; Ade, H.; Ma, W.; Yan, H. *Nat. Energy* **2016**, *1*, 15027.

(29) Li, Y.; Liu, X.; Wu, F.-P.; Zhou, Y.; Jiang, Z.-Q.; Song, B.; Xia, Y.; Zhang, Z.-G.; Gao, F.; Inganäs, O.; Li, Y.; Liao, L.-S. *J. Mater. Chem. A* **2016**, *4*, 5890−5897.

(30) Liang, N.; Meng, D.; Ma, Z.; Kan, B.; Meng, X.; Zheng, Z.; Jiang, W.; Li, Y.; Wan, X.; Hou, J.; Ma, W.; Chen, Y.; Wang, Z. *Adv. Energy Mater.* **2017**, *7*, 1601664.

(31) Li, S.; Liu, W.; Shi, M.; Mai, J.; Lau, T.-K.; Wan, J.; Lu, X.; Li, C.-Z.; Chen, H. *Energy Environ. Sci.* **2016**, *9*, 604−610.

(32) Liu, W.; Li, S.; Huang, J.; Yang, S.; Chen, J.; Zuo, L.; Shi, M.; Zhan, X.; Li, C. Z.; Chen, H. *Adv. Mater.* **2016**, *28*, 9729−9734.

(33) Chen, S.; Zhang, G.; Liu, J.; Yao, H.; Zhang, J.; Ma, T.; Li, Z.; Yan, H. *Adv. Mater.* **2017**, *29*, 1604231.

(34) Lin, Y.; Wang, J.; Zhang, Z. G.; Bai, H.; Li, Y.; Zhu, D.; Zhan, X. *Adv. Mater.* **2015**, *27*, 1170−1174.

(35) Lin, Y.; Zhang, Z.-G.; Bai, H.; Wang, J.; Yao, Y.; Li, Y.; Zhu, D.; Zhan, X. *Energy Environ. Sci.* **2015**, *8*, 610−616.

(36) Li, S.; Ye, L.; Zhao, W.; Zhang, S.; Mukherjee, S.; Ade, H.; Hou, J. *Adv. Mater.* **2016**, *28*, 9423−9429.

(37) Li, M.; Ni, W.; Feng, H.; Wan, X.; Liu, Y.; Zuo, Y.; Kan, B.; Zhang, Q.; Chen, Y. *Org. Electron.* **2015**, *24*, 89−95.

(38) Park, S. H.; Roy, A.; Beaupre, S.; Cho, S.; Coates, N.; Moon, J. S.; Moses, D.; Leclerc, M.; Lee, K.; Heeger, A. J. *Nat. Photonics* **2009**, *3*, 297−302.

(39) Li, P.; Tong, H.; Liu, J.; Ding, J.; Xie, Z.; Wang, L. *RSC Adv.* **2013**, *3*, 23098.

(40) Inganas, O.; Zhang, F.; Tvingstedt, K.; Andersson, L. M.; Hellstrom, S.; Andersson, M. R. *Adv. Mater.* **2010**, *22*, E100−116.

(41) Keshtov, M. L.; Kuklin, S. A.; Chen, F. C.; Khokhlov, A. R.; Peregudov, A. S.; Siddiqui, S. A.; Sharma, G. D. *Org. Electron.* **2015**, *24*, 137−146.

(42) Zhou, P.; Dang, D.; Xiao, M.; Wang, Q.; Zhong, J.; Tan, H.; Pei, Y.; Yang, R.; Zhu, W. *J. Mater. Chem. A* **2015**, *3*, 10883−10889.

(43) Cui, Y.; Xu, B.; Yang, B.; Yao, H.; Li, S.; Hou, J. *Macromolecules* **2016**, *49*, 8126−8133.

(44) Zhang, X.; Zhan, C.; Yao, J. *Chem. Mater.* **2015**, *27*, 166−173.

(45) Kan, B.; Zhang, Q.; Li, M.; Wan, X.; Ni, W.; Long, G.; Wang, Y.; Yang, X.; Feng, H.; Chen, Y. *J. Am. Chem. Soc.* **2014**, *136*, 15529−15532.

(46) Tang, H.; Lu, G.; Li, L.; Li, J.; Wang, Y.; Yang, X. *J. Mater. Chem.* **2010**, *20*, 683−688.

(47) Gilot, J.; Wienk, M. M.; Janssen, R. A. J. *Adv. Funct. Mater.* **2010**, *20*, 3904−3911.

(48) Bahro, D.; Koppitz, M.; Mertens, A.; Glaser, K.; Mescher, J.; Colsmann, A. *Adv. Energy Mater.* **2015**, *5*, 1501019.

(49) Beek, W. J. E.; Wienk, M. M.; Kemerink, M.; Yang, X. N.; Janssen, R. A. J. *J. Phys. Chem. B* **2005**, *109*, 9505−9516.

DOI: 10.1021/jacs.7b01493